Computed SAR and Thermal Elevation in a 0.25-mm 2-D Model of the Human Eye and Head in Response to an Implanted Retinal Stimulator—Part I: Models and Methods

Stephen C. DeMarco, Gianluca Lazzi, *Senior Member, IEEE*, Wentai Liu, *Senior Member, IEEE*, James D. Weiland, *Member, IEEE*, and Mark S. Humayun, *Member, IEEE*

***Abstract*—Retinitis pigmentosa and age-related macular degeneration lead to blindness through progressive loss of retinal photoreceptors. Attempts are under way to construct a visual prosthesis to recover a limited sense of vision for these patients with the aid of implantable electronic devices. The function of these microchips is to provide electrical stimulation to existing viable retinal tissues—living ganglion and bipolar cells—using an array of on-chip stimulus circuits, while the dominant mechanism for power and data communication for these implanted devices has been wireless inductive telemetry using coils. This paper describes methods and models used to estimate the heating induced in the human eye and surrounding head tissues subject to the operation of this retinal prosthesis. A two-dimensional 0.25-mm high-resolution human head model has been developed with the aid of a new semiautomatic graphical segmentation algorithm. Finite-difference-based numerical methods for both electromagnetic and thermal modeling have been used to determine the influence of the specific absorption rate (associated with 2-MHz inductive coupling to the implant) and of stimulator integrated circuit (IC) power on tissue heating under different operational conditions and different hypothesis on choroidal blood flow and properties of the complex implanted circuitry. Results, provided in Part II of this paper, show that temperature increases of approximately 0.6 and 0.4°C are induced in the midvitreous of the human eye in the absence and presence of choroidal blood flow, respectively, for a 60-electrode retinal prosthesis chip. Correspondent temperature rises of approximately 0.19 and 0.004 °C on the retina are obtained for these cases. Comparison with in vivo experimental measurements on intraocular heating in dog eyes shows good agreement.**

***Index Terms*—Age-related macular degeneration, finite-difference time domain (FDTD), retina prosthesis, retinitis pigmentosa, specific absorption rate (SAR), stimulator IC, temperature, thermal simulation.**

Manuscript received November 1, 2001; revised June 3, 2002. The work of G. Lazzi was supported in part by the Whitaker Foundation under Contract RG-00-0298 and in part by NSF CAREER Award ECS-0091599. The work of W. Liu was supported in part by NSF Award BES-9808040 and in part by the National Institutes of Health (NIH). The work of J. D. Weiland and M. S. Humayun was supported in part by NSF Award BES-9810914 and in part by NIH.

S. C. DeMarco, G. Lazzi, and W. Liu are with the Department of Electrical and Computer Engineering, North Carolina State University, Raleigh, NC 27695 USA.

J. D. Weiland and M. S. Humayun are with Doheny Eye Institute, University of Southern California, Los Angeles, CA 90089 USA.

Digital Object Identifier 10.1109/TAP.2003.816395

I. Introduction

AGE-RELATED macular degeneration (AMD) and retinitis pigmentosa (RP), among the leading causes of blindness [1], affect over 10 million people worldwide through progressive photoreceptor loss (rod/cones) in the retina [2], [3]. The photoreceptor cells in a healthy retina initiate a neural signal in response to incident light. This neural signal is further processed by bipolar and ganglion cells of the inner retina prior to delivery to higher visual processing areas in the cortex. Retinal photoreceptors are almost completely absent in the retina of end-stage RP and AMD patients, while the bipolar cell and ganglion cells, through which the photoreceptors normally synapse, may survive at higher rates [4], [5]. The ganglion and bipolar cells remain intact, and due to the anatomy of the retina, they are in a position where they may respond to artificially induced electrical stimulation via an implant. The demonstration that direct electrical stimulation of retinal ganglion cells can create visual sensation in patients has been shown clinically [6], [7]. Patients have been able to recognize English characters and other simple forms when stimulated by a small array of retinal electrodes. This opens the possibility of an electronic prosthesis to bypass the defective photoreceptors.

A conceptual schematic of the retinal prosthesis system is given in Fig. 1. It consists of two units, extraocular and intraocular. The extraocular unit includes a camera for the collection of images, a data encoding chip for the discretization of the image in an 8×8 pixelized data set, and a telemetry coil for the transmission of power and data to the intraocular unit. The latter unit consists of a receiving telemetry coil, a power and signal transceiver and processing chip, a stimulation current driver, and a stimulating electrode array mounted on the retina. The 5.5×5.25 mm stimulator chip occupies a central position within the eyeball so as to better isolate its heat and mechanical stresses from the sensitive retina, while the stimulus currents are delivered to the retinal surface via the electrode array.

As with all implantable electronic devices, the operation of the retinal prosthesis implanted in a human patient is expected to bring about an increase in the natural steady-state temperature of the eye and surrounding head tissues. Therefore, a study is undertaken via numerical simulation to predict the extent of temperature increase due to the operation of the retinal prosthesis.

0018-926X/03$17.00 © 2003 IEEE

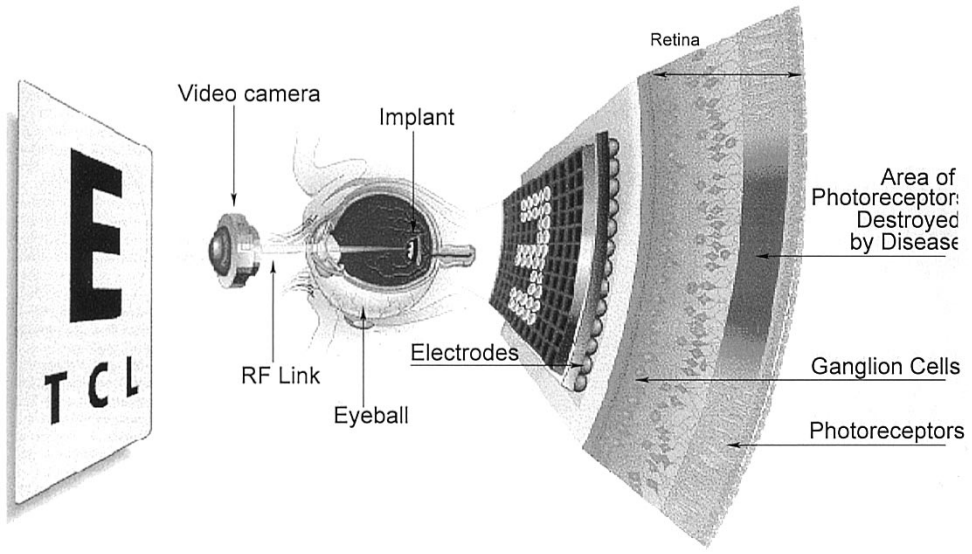

Fig. 1. Block diagram for the retina prosthesis system.

Ocular heating is being accounted for in terms of inductive powering (for which we quantify the specific absorption rate of electromagnetic power deposition) and the power dissipation in an implantable retinal stimulator microchip positioned at midvitreous. Although the prosthesis will consist of additional components, including the receiving coil and mechanical support structures, our thermal studies are limited at this time to the specific absorption rate (SAR) associated with inductive coupling and the power consumption in the implanted chip itself.

In recent years, studies and results have been reported in which the temperature increases in the head are of interest. Many of these have been brought about from the proliferation of cellular phones and concerns of their influence on the human head [8]–[10]. Furthermore, supposed links between electromagnetic exposure and the formation of cataracts [11], [12] have led to increased interest in studies of thermal heating in the human eye due to radiation in wireless computer networks [13], from infrared radiation in industrial settings [14], and to forms of electromagnetic exposure [15]. These studies have been primarily conducted at frequencies in the vicinity of 700 MHz to 2.45 Ghz, due to the proliferation of wireless devices operating in these bands.

In this paper, we describe methods and models used to compute estimates of heating in the human eye and surrounding head tissues subjected to the operation of such a retinal prosthesis. Electromagnetic power deposition resulting from inductive telemetry and power dissipation from the implanted stimulator IC are the heating mechanisms that are characterized.

This paper is organized into seven major sections. A review of the numerical finite-difference time-domain (FDTD) and thermal methods is presented in Section II, accompanied by a validation of the numerical methods against analytical derivations. Section III offers comments on scaling considerations for modeling $\vec{\mathbf{E}}/\vec{\mathbf{H}}$-field distribution from the three-dimensional (3-D) transmitter coil in 2-D simulation. The mathematical modeling of power dissipation in the stimulator IC for use in the numerical thermal method is formulated in Section IV and computed in Section V. A discussion of human head and eye model generation and the properties of the biological tissues is provided in Sections VI and VII, respectively. The SAR and thermal simulation results are presented in Part II of this paper, along with validation according to measured data from physical thermal experiments.

II. Computational Methods

In order to reduce the computational complexity, the amount of required memory, and the simulation time, simulations of electromagnetic deposition and thermal elevation in the human head are conducted in two dimensions. In fact, it is possible to approximate the fields generated by the 3-D transmitter coil used for inductive telemetry (as in the head/eye simulations for the retinal prosthesis) via two sources of opposite polarity normal to a plane passing through the center of the coil and coplanar with the coil axis.

A 2-D D-H transverse magnetic (TM) formulation of the FDTD method has been used to compute the induced electromagnetic energy in a 0.25-mm resolution head model derived from the visible man project (see Section VI). This D-H formulation has the advantage that the perfectly matched layer (PML) absorbing boundary conditions are independent from the background dielectric materials in the FDTD mesh (both in 2-D and 3-D formulations), thus allowing the truncation of the head model as described in [16] in order to limit the computational space. The development of the method closely parallels that in [16] and [17] and for the sake of brevity will not be repeated here.

The thermal elevation in biological tissue can be computed by means of the bioheat conduction equation [13], which includes the heating effect of basal metabolism A_0 and the cooling effect of blood perfusion B in the tissues. For tissue irradiated electromagnetically, the bioheat equation is further expanded to account for the heating effect of SAR, which is a measure of absorbed power per unit mass of tissue due to exposure to electromagnetic fields and is expressed as $\mathrm{SAR} = (\sigma \|\vec{\mathbf{E}}\|^2)/(2\rho)$ in $[\mathrm{W/kg}]$, for conductivity σ, electric field $\vec{\mathbf{E}}$, and mass density ρ.

Furthermore, the dissipated power of the implanted stimulator IC $P_{\mathrm{chip(3-D)}}$ is also expected to raise tissue temperature, and is included as a power density in the continuous space with units of W/m^3. The resulting expanded *bioheat* equation is given as

$$C\rho\frac{\partial T}{\partial t}=K\nabla^2 T+A_0-B(T-T_b)+\rho\mathrm{SAR}+P^{(\mathrm{density})}_{\underset{(\underline{\mathbf{continuous}})}{\mathrm{chip(3-D)}}}\left[\frac{\mathrm{W}}{\mathrm{m}^3}\right] \tag{1}$$

where $K\nabla^2 T$ is the thermal spatial diffusion term[1] for Celsius temperature T, thermal conductivity K, specific heat C, mass density ρ, and blood temperature T_b, assumed constant at 37 °C.

At the boundary of the tissue where the surrounding environment is encountered, the conduction of heat through the tissue arriving at the boundary normal to the surface must match the convective transfer of heat into the environment [13]. The exchange of heat with the surrounding environment is proportional to the difference between the surface temperature and the environmental temperature [8], [13] as given in (2)

$$K\frac{\partial T}{\partial n}(x,y,z)=-H_a\left(T_{(x,y,z)}-T_a\right)\quad\left[\frac{\mathrm{W}}{\mathrm{m}^2}\right] \tag{2}$$

where $T(x,y,z)$ is evaluated on the surface, n is the surface normal, H_a is the convection coefficient for heat exchange with the environmental ambient temperature with a value of 20 J/m^{2}s °C [13], and T_a is the surrounding ambient temperature, assumed constant at 24 °C. Based on the derivation from [13], (1) and (2) are spatially/temporally discretized and combined as in (3) for simulation on the 2-D head/eye model, developed in Section VI. In particular, the SAR and stimulator IC power dissipation density are now expressed as 2-D quantities in the discretized space

$$\begin{aligned}T^{n+1}_{(i,j)}=&\frac{K\delta t}{\rho C\delta x^2}\left(T^n_{(i-1,j)}+T^n_{(i+1,j)}+T^n_{(i,j-1)}+T^n_{(i,j+1)}\right)\\&+\frac{\delta t}{\rho C}\left[\rho\mathrm{SAR}_{(i,j)}+P^{(\mathrm{density})}_{\underset{(\underline{\mathbf{discrete}})}{\mathrm{chip(3D)}}}(i,j)+A_{0_{(i,j)}}+B_{(i,j)}T_b\right]\\&+T^n_{(i,j)}\left[1-\left(N_{\mathrm{INT}}\frac{K}{\rho C\delta x^2}+N_{\mathrm{EXT}}\frac{H}{\rho C\delta x}+\frac{B}{\rho C}\right)\delta t\right]\\&+N_{\mathrm{EXT}}\frac{H\delta_t T_a}{\rho C\delta x}[^\circ C]\end{aligned} \tag{3}$$

where N_{INT} is the number of interior points adjacent to cell (i, j) and N_{EXT} is the number of exterior points adjacent to cell (i, j) (i.e., those outside of the model and belonging to the surrounding environment). The maximum time step to ensure stability of the algorithm is considered as the minimum value of the expression of (4) [13], evaluated for all tissues and materials present in the discretized head/eye model

$$\delta_t\le\min_{m\epsilon M}\left(\frac{1}{\frac{N_{\mathrm{INT}}K_m}{\rho_m C_m\delta x^2}+\frac{N_{\mathrm{EXT}}H}{\rho_m C_m\delta x}+\frac{B_m}{\rho_m C_m}}\right) \tag{4}$$

where M is the set of tissues.

Equations (3) and (4) are used to calculate the temperature rise in the eye when exposed to electromagnetic radiation from inductive coupling and to power dissipation from the implanted stimulator microchip. The parameters used in these equations together with their units are summarized in Table I.

TABLE I
PARAMETERS OF THE DISCRETIZED BIOHEAT EQUATION

Symbol	Physical Property	Units
T	Temperature	°C
t	continuous time	s
n	surface normal	–
ρ	mass density	$\left[\frac{\mathrm{kg}}{\mathrm{m}^3}\right]$
C	specific heat	$\left[\frac{\mathrm{J}}{\mathrm{kg\,°C}}\right]$
K	thermal conductivity	$\left[\frac{\mathrm{J}}{\mathrm{m\,s\,°C}}\right]$
H_a	convective transfer coefficient (for ambient environment temperature)	$\left[\frac{\mathrm{J}}{\mathrm{m^2 s\,°C}}\right]$
A_0	basal metabolic rate	$\left[\frac{\mathrm{J}}{\mathrm{m^3 s}}\right]$
B	blood perfusion coefficient	$\left[\frac{\mathrm{J}}{\mathrm{m^3 s\,°C}}\right]$
T_b	blood temperature (constant)	°C
T_a	environment (ambient) temperature (constant)	°C
δx	spatial step (resolution) in the x, i direction	m
δy	spatial step (resolution) in the y, j direction	m
δz	spatial step (resolution) in the z, k direction	m
δt	discretized time step	s
SAR	specific absorption rate	$\left[\frac{\mathrm{W}}{\mathrm{kg}}\right]$
$P^{(density)}_{chip(2D)\,(discrete)}(i,j)$	2D power dissipation density	$\left[\frac{\mathrm{W}}{\mathrm{m}^3}\right]$
$P_{chip(3D)}$	stimulator IC power dissipation in 3D	W

The accuracy of the implemented methods has been verified against the analytical solution for the specific absorption rate and the thermal response associated with a plane wave impacting a solid lossy cylinder, derived in [18]. The validation of our FDTD and thermal implementations is performed at the frequency of 2.45 GHz reported in [18], in order to compare with the published results, as well as at 2 MHz, which is the operating frequency of the extraocular transmitting coil used to inductively power the implanted microstimulator. An excellent agreement between numerical and analytical results is obtained for both frequencies. Fig. 2(a) shows analytical and numerically computed temperature in a 10-cm-diameter cylinder exposed to a plane wave of power density 10 mW/cm^2 at a frequency of 2 MHz. The curves report the temperature at various time intervals subsequent to the initial irradiation time, along the diameter of the cylinder, which is perpendicular to the direction of propagation of the incident plane wave. The computed 2-D pattern is shown in Fig. 2(b).

III. Modeling of the Extraocular Coil

As the simulations of temperature increase in the head/eye model developed here are conducted in two dimensions, special treatment is required for the transmitter coil. The current

[1]As we are interested in temperature increases in the midvitreous (and not internal chip temperature), we have used the term $K\nabla^2 T$ instead of the more generalized $\nabla(K\nabla T)$. In fact, a number of 2- and 3-D numerical tests of the chip model positioned in the center of a cylinder or a sphere have shown that the use of the thermal diffusion term $K\nabla^2 T$ in lieu of $\nabla(K\nabla T)$ in the 2-D modeling of the implanted microchip provides temperature increases that are in better agreement with those obtained outside the chip by 3-D simulations employing the term $\nabla(K\nabla T)$.

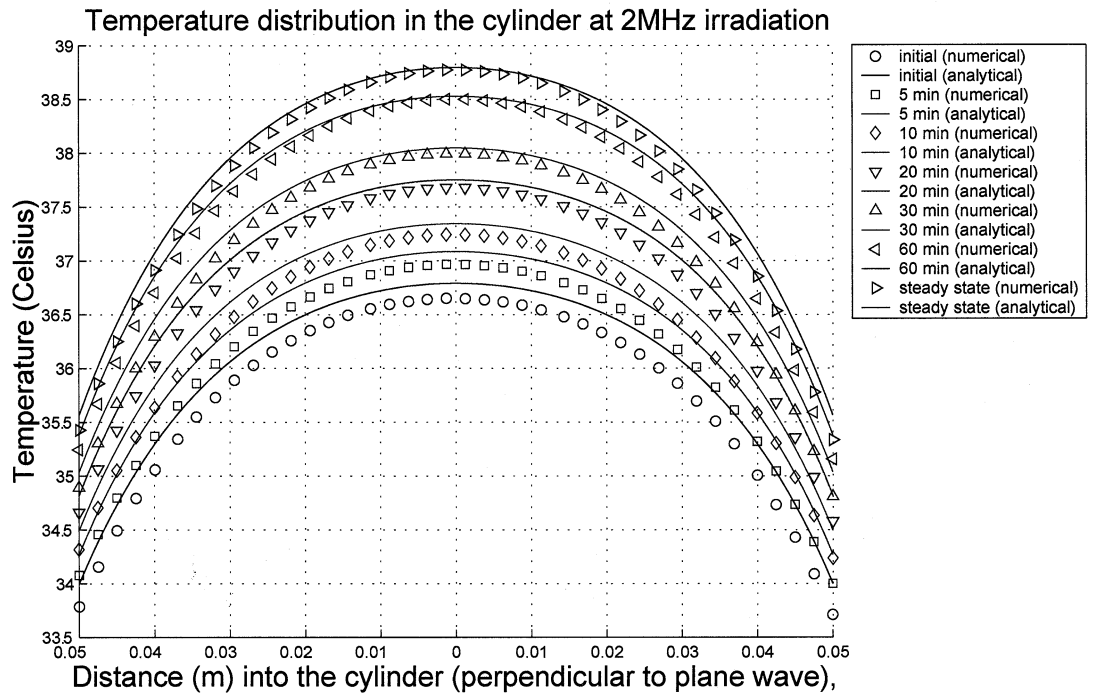

(a)

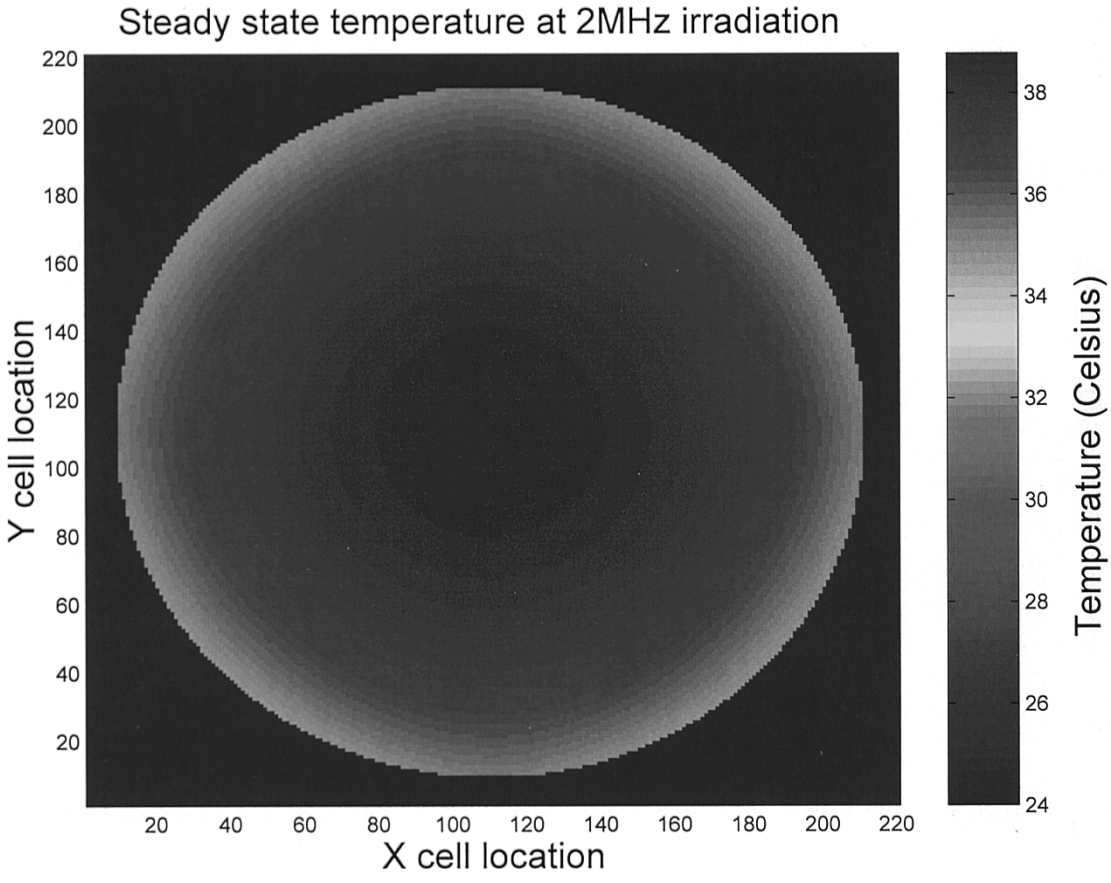

(b)

Fig. 2. Temperature distribution in the test cylinder at 2-MHz irradiation. (a) Comparison of analytically and numerically computed temperature. (b) Numerically computed temperature distribution.

version of the telemetry system includes an extraocular transmitting multiturn coil of 2-in diameter located at a distance of approximately 2 cm from the human eye, and an intraocular receiving multiturn coil of 7-mm diameter that replaces the human lens. The extraocular coil needs to carry a current of 2 A to deliver the necessary power to the intraocular unit.

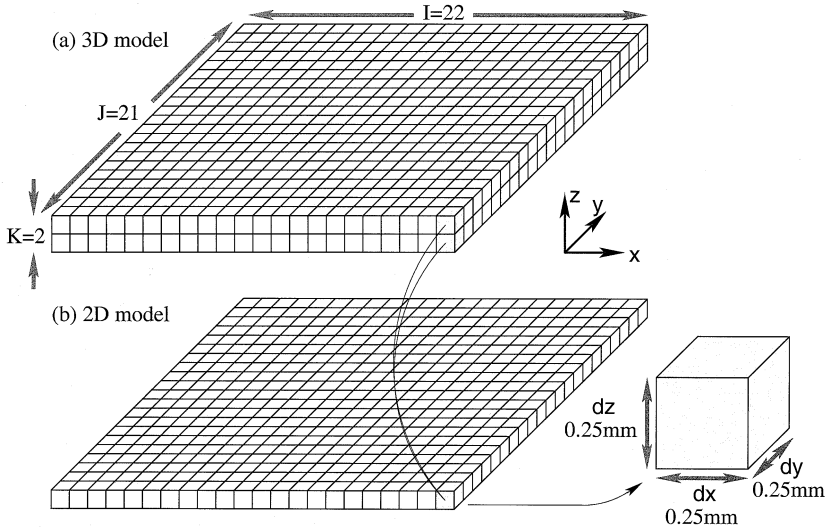

Fig. 3. *Retina-3.5* stimulator IC models discretized to 0.25-mm uniform spatial resolution.

For a low-frequency 3-D coil of radius R, and turns count, N, carrying a current of I, we can consider the magnetic field $\vec{\mathbf{H}}$ as given by $||\vec{\mathbf{H}}|| = (NI)/(2R)$. The coil current in a 3-D model space would be approximated with a finite number of tangential current vectors positioned around the circumference of the coil. However, for performing 2-D simulations, the coil current is represented with two parallel and tangential current vectors of opposite polarity.

This approximation requires that the theoretical value of $\vec{\mathbf{H}}$ at the center of the multiturn external coil in the 2-D sense be scaled to that of the magnetic field at the center of the real, 3-D coil model. Even though the 2-D and 3-D cases are characterized by different rates of decay of the electromagnetic field. This has been verified by means of 2-D and 3-D FDTD simulations as well as by comparing analytical solutions of the electromagnetic fields generated in free space by the 2-D and 3-D approximations of the radiating device [19].

IV. Modeling Power Dissipation in the Stimulator IC

Modeling of the stimulator microchip also requires approximations that allow us to correctly represent the power dissipated by the chip in a 2-D space, rather than 3-D. MOSIS reports the die size for our *Retina-3.5* stimulator IC [20] in the AMI-1.2 μm process as 4.7 mm $\times$ 4.6 mm $\times$ 500 μm. However, after accounting for clearance around the pad-ring for the wafer dicing saw, the die size becomes 5.53 mm $\times$ 5.25 mm $\times$ 508 μm.

Discretizing this chip volume to 0.25-mm spatial resolution yields the 3-D chip model shown in Fig. 3(a) with cellular dimensions $I = 22 \times J = 21 \times K = 2$, with the total power dissipation expressed as a volume summation of the discrete power density $P^{(\text{density})}_{\underset{(\mathbf{discrete})}{\text{chip(3-D)}}}(i,j,k)$, as given in

$$P_{\text{chip(3-D)}} = \sum_{i=1}^{I}\sum_{j=1}^{J}\sum_{k=1}^{K} P^{(\text{density})}_{\underset{(\mathbf{discrete})}{\text{chip(3D)}}}(i,j,k). \tag{5}$$

When considering a 2-D model of the 3-D stimulator chip for thermal simulation in the 2-D head/eye model of Fig. 8, the total power $P^{(\text{density})}_{\text{chip(3-D)}}$ is retained by integrating (or summing) the power density for the 3-D chip model along the k-axis for each cell (i, j) in the 2-D chip model. Although this yields power density units in 2-D of W/m^2, we consider that the 2-D model shown in Fig. 3(b) can be conceptually extended infinitely in the k-dimension. Therefore units of W/m^3 are retained in the 2-D chip model for the power density at (i, j) consistent with the units of the tissue properties, such as mass density ρ in kg/m^3. This means of condensing the power density is formulated as

$$P^{(\text{density})}_{\underset{(\mathbf{discrete})}{\text{chip(3-D)}}}(i,j) = \sum_{k=1}^{K} P^{(\text{density})}_{\underset{(\mathbf{discrete})}{\text{chip(3-D)}}}(i,j,k). \tag{6}$$

In general, the power density varies across a chip, but in the case of our *Retina-3.5* stimulator, the IC [20] consists of an array of 60 identical stimulus current driver circuits, which are uniformly distributed over 75% of the chip area (25% is occupied by digital control circuits). Thus, we approximate the power density as uniformly distributed, such that

$$P^{(\text{density})}_{\underset{(\mathbf{discrete})}{\text{chip(3-D)}}}(i,j) = \sum_{k=1}^{K} \frac{P_{\text{chip(3-D)}}}{(Idx)(Jdy)(Kdz)} \tag{7}$$

where $dx = dy = dz = 0.25$ mm, and $I = 22$, $J = 21$, and $K = 2$. The power density $P^{(\text{density})}_{\underset{(\mathbf{discrete})}{\text{chip(2-D)}}}(i,j)$, as defined here and associated with the 2-D chip model of Fig. 3(b), is the same value used in the 2-D bioheat formulation of (3).

V. Computing Power Dissipation in the Stimulator IC

The 60 stimulus circuits of our *Retina-3.5* stimulator IC [20] provide biphasic current outputs for retinal stimulation, with programmable amplitudes, pulse widths, and pulse rate. The power consumption associated with operating the microstimulator can be accounted for in terms of the power dissipated in the retinal tissue (the *load*) plus additional power overhead required by the microstimulator IC. This is expressed in (8) for instantaneous power as a function of time, where the superscript "60" in parentheses refers to the case where all 60 stimulation channels

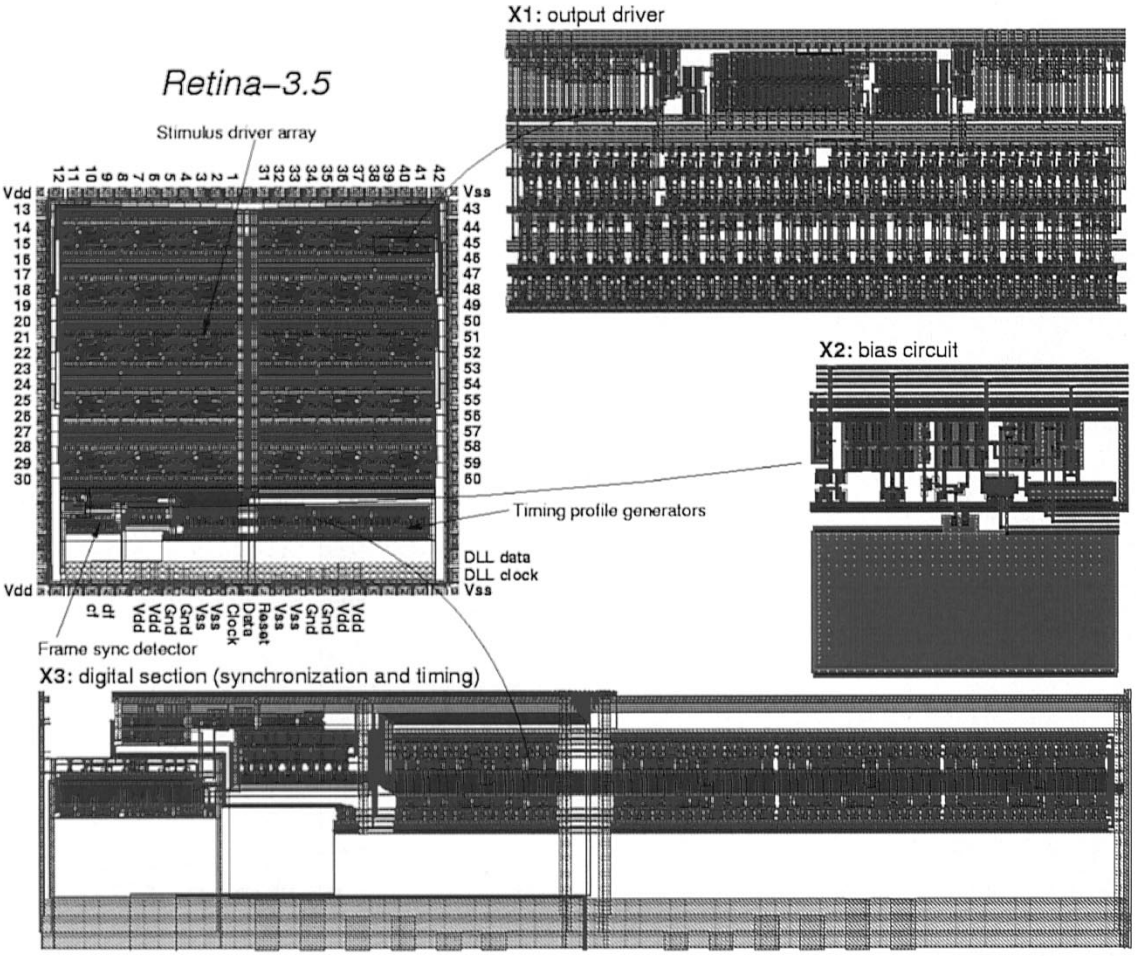

Fig. 4. *Retina-3.5* stimulator IC layouts simulated in *HSPICE* to determine power dissipation.

are active. The subscripts *chip*, *load*, and *consumed* refer to the power consumed in the microstimulator, retinal tissue, and the combined system, respectively

$$P^{(60)}_{\text{consumed}}(t) = P^{(60)}_{\text{chip}}(t) + P^{(60)}_{\text{load}}(t). \tag{8}$$

A. Simulated Power Dissipation in the Stimulator IC

Since the *Retina-3.5* stimulator IC [20] layout contains nearly 70 000 field-effect transistors, circuit simulators such as *HSPICE* cannot practically conduct chip-level simulations that cover milliseconds of real time. However, the array of stimulus circuits accounts for the majority of the area on our IC (about 75%). Therefore, a reasonable estimate of the dissipated power of the chip can be formulated from a simulation of a single output driver (one from the array of 60), the biasing circuit (which manifests static power dissipation), and the digital section (associated with packet synchronization and timing generation), designated as subcircuits X1, X2, and X3, respectively, as illustrated in Fig. 4.

In simulation, the output driver of subcircuit X1 is loaded with a resistance $R_{\text{load}} = 10\ \text{k}\Omega$ to model retinal impedance [21]. The power dissipation of the chip could be predicted from the simulated estimates of subcircuits X1–X3, designated $P_{\text{X1}}-P_{\text{X3}}$ as in (9), excluding the power, P_{load}, dissipated in R_{load}, which is off chip

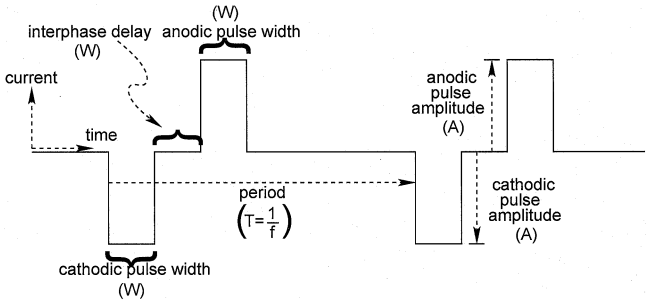

Fig. 5. Parameters of the biphasic current pulse used for retinal stimulation.

$$P_{\text{chip(3-D)}} = P^{(60)}_{\text{chip}} = 60(P_{\text{X1}}) + P_{\text{X2}} + P_{\text{X3}}. \tag{9}$$

In simulating the power requirements of the stimulator IC, the standard biphasic current pulse for retinal stimulation is considered as reported in [7] and shown in Fig. 5. The microstimulator is programmed to produce this current waveform on all 60 output channels simultaneously. Equal anodic and cathodic currents of 400-μA (the typical case) and 600-μA (the worse or maximum case) for *Retina-3.5* are considered, with V_{dd} and V_{ss}

TABLE II
HSPICE SIMULATED POWER DISSIPATION FOR OUR *Retina-3.5* IC RESULTING FROM VARIATIONS IN BIPHASIC STIMULUS

V_{dd}, V_{ss} [V_{DC}]	current A [μA]	frame rate[2] f = $\frac{1}{T}$ [Hz]	pulse width[3] W [ms]	bias power P_{X1} [mW]	driver power P_{X2} [mW]	load power P_{load} [mW]	driver power×60 $P_{X2}\times60$ [mW]	load power×60 $P_{load}\times60$ [mW]	digital power P_{X3} [mW]	chip power[4] $P_{chip}^{(60)}$ [mW]
+5, −5	400 [1]	50	1	2.4700	0.1041	0.1633	6.2436	9.8004	0.4726	9.1862
+5, −5	400 [1]	50	2	2.4700	0.2036	0.3251	12.2154	19.5066	0.4726	15.1580
+5, −5	400 [1]	50	3	2.4700	0.3041	0.4884	18.2448	29.3070	0.4726	21.1874
+5, −5	400 [1]	60	1	2.4700	0.1243	0.1951	7.4562	11.7030	0.4750	10.4012
+5, −5	400 [1]	60	2	2.4700	0.2443	0.3901	14.6568	23.4066	0.4750	17.6018
+5, −5	400 [1]	60	3	2.4700	0.3643	0.5852	21.8568	35.1102	0.4750	24.8018
+7, −7	600 [2]	50	1	3.5647	0.2043	0.3310	12.2604	19.8618	0.4964	16.3216
+7, −7	600 [2]	50	2	3.5647	0.3962	0.6589	23.7696	39.5310	0.4964	27.8308
+7, −7	600 [2]	50	3	3.5647	0.5899	0.9899	35.3916	59.3928	0.4964	39.4527
+7, −7	600 [2]	60	1	3.5647	0.2441	0.3953	14.6448	23.7174	0.5017	18.7112
+7, −7	600 [2]	60	2	3.5647	0.4754	0.7906	28.5228	47.4354	0.5017	32.5892
+7, −7	600 [2]	60	3	3.5647	0.7067	1.1859	42.4008	71.1540	0.5017	46.4672

[1] Anodic and cathodic pulse amplitudes resulting from *HSPICE* simulation at $V_{dd} = +5$ v and $V_{ss} = -5$ v were +400.8 and −405.1 μA, respectively.

[2] Anodic and cathodic pulse amplitudes resulting from *HSPICE* simulation at $V_{dd} = +7$ v and $V_{ss} = -7$ v were +575.3 and −572.1 μA, respectively. The driver output stages on the stimulator IC transition from saturation to the linear region when attempting to provide 600 μA for $R_{\text{load}} = 10$ kΩ [21] with $V_{dd} = +7$ v and $V_{ss} = -7$ v. Therefore, actual currents fall short of the requested values.

[2] Actual frame rates are 49.827 and 60.048 Hz, derived from a 12-MHz oscillator on the extraocular communications processor, which controls stimulus timing.

[3] Actual pulse widths are 1.023, 2.046, and 2.991 ms for 50-Hz frame rate and 1.045, 2.025, and 3.004 ms for 60-Hz frame rate again derived from the 12-MHz oscillator.

[4] Excludes load power.

set at $+5/-5$v or $+7/-7$v for each case, respectively, as appropriate [7]. Pulse repetition rates of 50 and 60 Hz are considered in keeping with results of flicker fusion experiments reported in [7]. Anodic and cathodic pulse widths and interphase delay were kept equal and varied among 1, 2, and 3 ms, consistent with stimulation experiments also reported in [7].

These parameters are annotated as A, W, and T on the stimulus waveform of Fig. 5 representing current amplitude, pulse and interphase-delay width, and period, respectively.

The subcircuits of Fig. 4 were programmed to produce the biphasic stimulus pulse of Fig. 5 in each of the parametric combinations described (12 cases in all). Subsequently, *HSPICE* simulations were conducted to estimate the power dissipation of *Retina-3.5* when operating in each case. The results are tabulated in Table II.

When computing power estimates on semiconductor circuits *HSPICE* considers only the power lost, or dissipated. Therefore, the estimates of $\mathrm{P}_{\mathrm{chip}}^{(60)}$ from Table II are taken as losses which would give rise to heat, and are subsequently used for $P_{\text{chip}(3-\text{D})}$ in (7) to compute $P_{\underset{(\mathbf{discrete})}{\text{chip}(2-\text{D})}}^{(\text{density})}(i,j)$ for the thermal method in (3) to predict temperature increase in the 2-D head/eye model.

B. Experimental Validation of Power Consumption and Dissipation in the Stimulator IC

Experimental measurements of the microchip power consumption were taken to validate the *HSPICE* simulations of the IC layout. Recall that our stimulator IC operates from dual dc supply rails of V_{dd} and V_{ss} to produce the anodic and cathodic phases, respectively, with respect to a central ground return Gnd. Therefore, an experimental estimate of chip power can be inferred from a measurement of the power consumption minus power dissipation in the 60 loads, as in (10)

$$P_{\text{consumed}}^{(60)} = V_{dd}I_{dd}^{(60)} + V_{ss}I_{ss}^{(60)} - 60\frac{(V_{\text{load}})^2}{R_{\text{load}}} \qquad (10)$$

where I_{dd} and I_{ss} are the average supply currents for the V_{dd} and V_{ss} supplies and V_{load} is the rms voltage measured across the load resistance, $R_{\text{load}} = 10$ kΩ. Results of the measurement experiment along with the inferred microstimulator power are summarized in Table III. A comparison between the simulated and measured estimates for the chip power is included. The difference between the simulated and experimental estimates of the power dissipation varies by no more than about 2 mW, thus indicating that the experimental measurement is in good agreement with the simulated estimates.

VI. HEAD AND EYE COMPUTATIONAL MODELS

Since the determination of a detailed thermal distribution in the human eye is critical for the development of a safe retinal prosthesis implant, there is the need to develop a high-resolution 2-D head model that accurately accounts for all the anatomical features of the human eye. Since there are no available magnetic resonance images accurate enough to capture the finest anatomical details of the human eye, it has been necessary to derive the eye model from an anatomically accurate sketch of a human eye, taken from [22] and [23].

The sketch of the eye was electronically scanned to obtain an image of roughly 600 × 600 pixel resolution. Subsequently, the optic nerve and the muscles connecting to the sclera were removed, and the resulting image was color segmented according to the distinct tissues represented, as shown in Fig. 6(a).

A software application has been developed to discretize the segmented eye image onto a uniform grid of 0.25-mm resolution in order to sample it to a high resolution for construction of

TABLE III
EXPERIMENTALLY MEASURED POWER CONSUMPTION AND DISSIPATION IN OUR *Retina-3.5* IC RESULTING FROM VARIATIONS IN BIPHASIC STIMULUS

V_{dd}, V_{ss}[1] [V_{DC}]	current[2] A [μA]	frame rate f = $\frac{1}{T}$ [Hz]	pulse width W [ms]	measured consumption[3] $P^{(60)}_{consumed}$ [mW]	measured load power $P^{(60)}_{load}$ [mW]	inferred chip power[4] $P^{(60)}_{chip(measured)}$ [mW]	simulated chip power[5] $P^{(60)}_{chip(simulated)}$ [mW]
+5, −5	400	50	1 [4]	18.4818	11.3276	7.1541	9.1862
+5, −5	400	50	2 [4]	36.4597	20.8378	15.6219	15.1580
+5, −5	400	50	3 [4]	53.0817	28.7304	24.3513	21.1874
+5, −5	400	60	1 [5]	22.4489	11.6612	10.7877	10.4012
+5, −5	400	60	2 [5]	42.7871	22.8569	19.9302	17.6018
+5, −5	400	60	3 [5]	61.2672	33.6595	27.6076	24.8018

[1] Due to limitations in the current fabrication of our *Retina-3.5* stimulator IC, operation at $V_{dd} = +7$ v, $V_{ss} = -7$ v yields an amplitude imbalance measured between anodic and cathodic current when programmed to match. Therefore, experimentally measured power consumption and dissipation for validation with the simulated data of Table II were conducted only for the cases of $V_{dd} = +5$ v, $V_{ss} = -5$ v, which the matching is acceptable.

[2] Anodic and cathodic pulse amplitudes measured experimentally at $V_{dd} = +5$ v and $V_{ss} = -5$ v were 400 and -408μA, respectively.

[3] The resistance R_{series} placed in series with the power rails to facilitate experimental measurement of supply currents, I_{dd} and I_{ss}, is taken at a low value of 10.3 Ω. Therefore, the associated power dissipations, $(\Delta V_{dd})^2/R_{\text{series}}$ and $(\Delta V_{ss})^2/R_{\text{series}}$, are negligible and therefore not included in these measurements.

[4] Inferred from $P^{(60)}_{\text{chip}} = P^{(60)}_{\text{consumed}} - P^{(60)}_{\text{load}}$, which measures the difference in power consumed from the supplies and power dissipated in the 10-kΩ resistive loads when all 60 output drivers are active.

[5] Duplicated from Table II.

the model. At each cell in the overlying grid, the discretizer determines the dominant tissue type occupying that cell and identifies it according to the applied color segmentation. A unique tissue identifier is assigned to each cell location which is used as an index into a table of tissues (see Table IV) specifying dielectric and thermal properties. The resulting eye model that has been discretized to a spatial resolution of 0.25 mm is shown in Fig. 6(b).

A new 2-D head model was also constructed with a resolution of 0.25 mm suitable for an accurate representation of the finest anatomical details of the human head. The head model is derived from an image of the human head slice at a position intersecting the eyes, taken from the National Library of Medicine (NLM) *Visible Man Project* [24]. As with the eye model, construction of the head model proceeds by first color segmenting the head in order that tissues may be identified by uniform color. Subsequently, the discretizer is again used to sample the head slice image to a 0.25-mm model.

Since the eyes in the original head slice image from the *Visible Man Project* provide only two or three discernible tissues, the 0.25-mm resolution eye model separately developed is merged with the 0.25-mm head model to increase ocular detail as is shown in Fig. 7. A 2-D silicon model of the implanted stimulator IC of dimensions 5.5 mm $\times$ 5.25 mm is shown at midvitreous in the left eye, in the position and orientation associated with implantation.

It is expected that temperature increase arising from inductive coupling and from power dissipation in the stimulator IC will be localized to the region of the eyes. Therefore, in order to decrease the required memory and simulation time, the head/eye model is truncated posterior to the eyes as shown in Fig. 8.

When computing SAR, the posterior edge of the model is immersed in the PML layers in order to correctly support the model truncation for the reduction of the computational space, as explained in [16]. For the thermal simulation, instead, the initial steady-state temperature distribution, which is computed in the absence of any SAR and implant heating for the whole model, is forced along the posterior boundary in order to prevent inappropriate heat exchange with the surrounding environment. The model truncation is performed at a depth to which the conduction of internal heat is expected to be negligible.

VII. PHYSICAL PROPERTIES OF TISSUES

Dielectric and thermal property values have been taken from various publications collectively representing the research in electromagnetic and thermal dosimetry. The dielectric properties for the bodily tissues have been gathered from the Dielectric Properties of Body Tissues online database [25]. These data are compiled and organized by the Electromagnetic Wave Research Institute of the Italian National Research Council (IROE-CNR), based on the work of Gabriel [26]–[30] dating back to 1996. The permittivities and conductivities are evaluated at 2 MHz corresponding to the carrier frequency of the exterior transmitter coil in the inductive powering scheme. Thermal properties and specific gravities for the biological tissues have been collected primarily from [31] released in 1990, but also from other publications [8]–[10], [13], [15], [32]–[37]. Our *Retina-3.5* stimulator IC [20] fabricated in bulk CMOS is uniformly modeled with the physical properties of intrinsic silicon available from the online elemental database [38]. These properties used with the head/eye model are summarized in Table IV. As physical properties for some of the tissues are not explicitly available, values have been taken that match with tissues of nearest expected composition or water content.

The newly developed eye model accounts for sclera, cornea, aqueous humor, pupillary sphincter muscle, posterior chamber, crystalline lens, lens zonules, cilliary muscle, vitreous humor, choroid, and retina. Pupillary and cilliary muscles, lens zonules (likened to tendons), and muscles attached to the sclera are represented with the dielectric and thermal properties of generic human muscle. Due to its close proximity, the posterior chamber situated between the lens and pupillary muscle takes its properties from the aqueous humor. The permittivity and conductivity

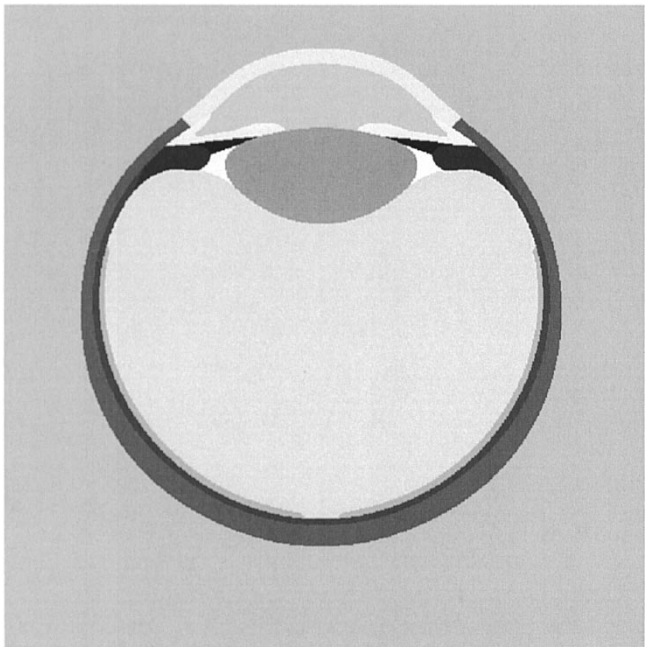

(a)

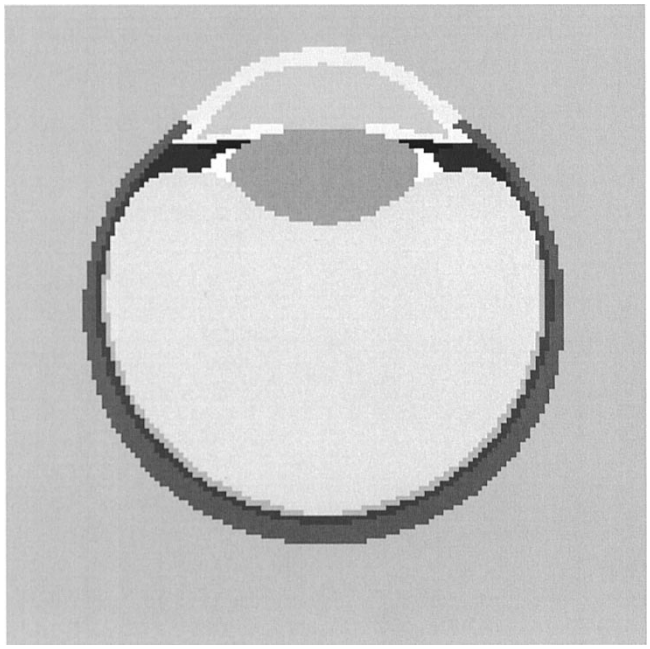

(b)

Fig. 6. Discretization to obtain the 0.25-mm 2-D eye model. (a) Color segmentation according to tissue type. (b) 2-D eye model sampled to 0.25 mm using a uniform grid.

of the aqueous humor at 2 MHz are taken as vitreous. Similarly, the mass density and thermal conductivity are shared among the aqueous and vitreous as [31] identifies a single humor for these two properties. Moreover, the specific heat properties are equal, as in [13]. The highly vascularized choroid, which lies between the retina and sclera and nourishes the photoreceptors, is approximated with the physical properties of blood.

[2]http://www.btinternet.com/ms_pages/whitematter.html.

[3]http://www.btinternet.com/ms_pages/greymatter.html.

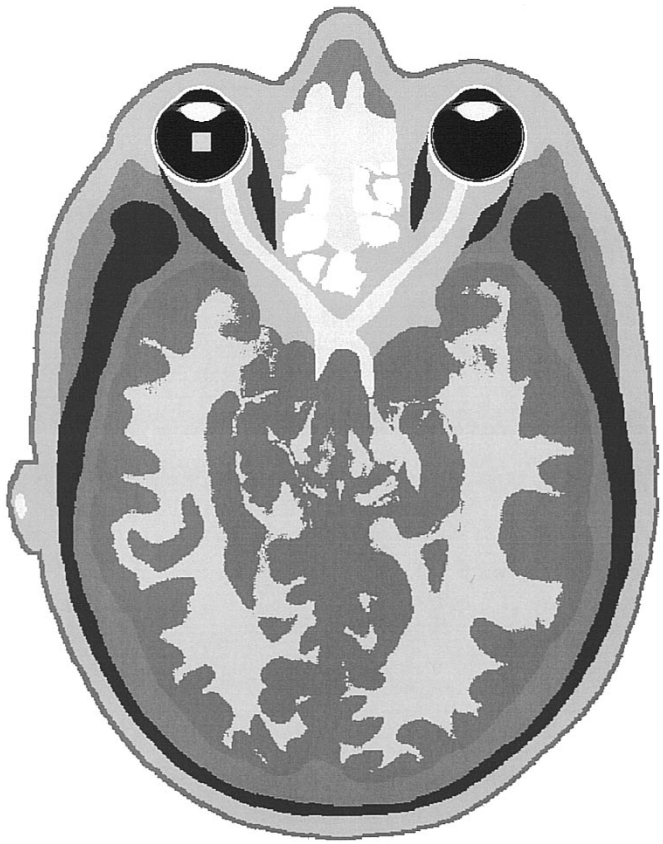

Fig. 7. Merged model of the discretized head and eye models with inclusion of the silicon stimulator IC model in the left eye.

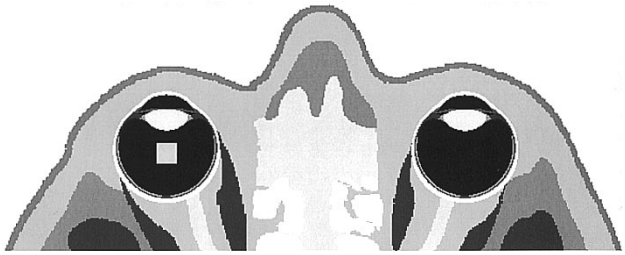

Fig. 8. Truncated model of the merged human head/eye models.

Only the dielectric properties of the retina have been found in available research literature [25]; mass density and thermal properties are not available. However, the retina is a multilayer neural structure approximately 300 μm thick with most of its composition organized as a cascade of various neuron cell types and their interconnections [22], [39]–[41]. Only in the innermost layer above the ganglion neurons is there a heavily axonal or nerve fiber layer. Therefore, in its composition, the retina is expected for the greater part to be analogous to brain gray matter, where there is a higher concentration of neural cell bodies and dendrites.

White matter represents the portion of brain neural structure involved in communication between areas of gray matter and thus has a high nerve fiber, or axonal, composition. Furthermore, as the optic nerves are reported to contain white matter, physical properties of nerve are assumed similar to those of white matter.

TABLE IV
DIELECTRIC AND THERMAL PROPERTIES OF TISSUES AND MATERIALS IN THE HEAD/EYE MODEL AT 2 MHz

Tissue	Relative Permittivity ε_R	Conductivity $\sigma\ [\frac{S}{m}]$	Mass Density $\rho\ [\frac{kg}{m^3}]$	Specific Heat $C\ [\frac{J}{kg\,°C}]$	Thermal Conductivity $K\ [\frac{J}{m\,s\,°C}]$	Blood Perfusion $B\ [\frac{J}{m^3\,s\,°C}]$	Metabolic Rate (Basal) $A_0\ [\frac{J}{m^3\,s}]$
air	1.000	0.0000	1.16	1300	0.250	0	0
muscle	826.000	0.5476	1040	3600 [20]	0.498 [12]	2700	690
deep fat	22.950	0.0255	920	2500 [20]	0.250 [13]	520	180
bone	106.000 [4]	0.0285 [4]	1810	1300 [8]	0.300 [14]	1000	0
cartilage	815.500	0.2776	1100	3400 [20]	0.450 [20]	9100	1000
skin	858.000	0.0371	1010	3500 [20]	0.420 [20]	9100	1000
nerve	554.800	0.1556	1043 [9]	3600 [9]	0.503 [9]	35000 [9]	10000 [9]
subcutaneous fat	22.950	0.0255	920	2500	0.250	520	180
brain grey matter	656.500	0.1807	1039 [18]	3680 [18]	0.565 [18]	35000	10000
brain white matter	340.600	0.1118	1043 [18]	3600 [18]	0.503 [18]	35000	10000
blood	1681.000	0.9261	1060	3840 [10]	0.530 [15]	–	0
sclera	1145.000	0.6889	1170	4178 [11]	0.580 [11]	0	0
scleral muscle [6]	826.000 [6]	0.5476 [6]	1040 [6]	3430 [6]	0.498 [6]	2700 [6]	690 [6]
cornea	1429.000	0.7438	1076 [18]	4178 [11]	0.580 [11]	0	0
pupillary muscle [6]	826.000 [6]	0.5476 [6]	1040 [6]	3430 [6]	0.498 [6]	2700 [6]	690 [6]
post chamber [5]	76.650 [5]	1.5010 [5]	1003 [5]	3997 [5]	0.578 [5]	0 [5]	0 [5]
lens	829.700	0.4170	1100	3000 [11]	0.400 [11]	0	0
lens zonules [6]	826.000 [6]	0.5476 [6]	1040 [6]	3430 [6]	0.498 [6]	2700 [6]	690 [6]
cilliary muscle [6]	826.000 [6]	0.5476 [6]	1040 [6]	3430 [6]	0.498 [6]	2700 [6]	690 [6]
aqueous humor	76.650 [17]	1.5010 [17]	1003 [18]	3997 [19]	0.578 [18]	0	0
vitreous humor	76.650	1.5010	1009 [18]	3997 [19]	0.594 [18]	0	0
choroid [7]	1681.000 [7]	0.9261 [7]	1060 [7]	3840 [7]	0.530 [7]	0 [7]	0 [7]
retina	1145.000	0.6889	1039 [16]	3680 [16]	0.565 [16]	35000 [16]	10000 [16]
silicon	– [21]	– [21]	2330 [22]	959 [22]	150.000 [23]	–	–

[1] Dielectric properties ε_R and σ are taken from [25] unless otherwise noted.

[2] Mass density ρ taken from [10] unless otherwise noted.

[3] Blood perfusion constant B and basal metabolic rate A_0 are taken from [9] unless otherwise noted.

[4] Cortical bone, taken from [25].

[5] Unavailable explicitly. Therefore, assigned the properties of aqueous humor.

[6] Taken as muscle (generic).

[7] Modeled as blood.

[8] Human cortical bone, taken from [31].

[9] Unavailable explicitly. Therefore, assigned the properties of brain white matter, as this is reported to have a high nerve fiber makeup and is contained in the optic nerves.[2]

[10] Human whole blood.

[11] Taken from [13].

[12] Human skeletal muscle, taken from [31].

[13] Averaged human subcutaneous fat, taken from [31].

[14] Taken from [8].

[15] Human whole blood (43 % Hct), taken from [31].

[16] Unavailable explicitly. Therefore, assigned the properties of brain gray matter, as this is reported to have a higher concentration of neural cell bodies and dendrites than white matter.[3]

[17] Unavailable explicitly. Therefore, assigned the properties of Vitreous Humor

[18] Taken from [31].

[19] Taken as Humor from [13].

[20] Taken from [9].

[21] Silicon not used in the calculation of the specific absorption rate.

[22] Taken from [38].

[23] The thermal conductivity of the implant is dependent on the precise material composition of the stimulator IC, any additional supporting intraocular components, and the hermetically sealed biocompatible casing. Therefore, thermal simulations were conducted with values of $K_{\text{chip}} \in \{10, 20, 30, \ldots, 80, 90\}$, so as to characterize the dependence of temperature increase on the chip's thermal conductivity. Subsequently, in order to minimize the computational time, temperature rise associated with $K_{\text{SI}} = 150$ (corresponding to the real value of silicon) are extrapolated according to the resulting trend.

Moreover, [9] and [42] report blood perfusion and basal metabolism in agreement with that of brain, or white matter. Hence, physical properties for nerve in Table IV are assigned from those explicitly available for white matter.

The thermal conductivity for the uniform silicon model of our *Retina-3.5* stimulator IC [20] is reported from [38] as 150 J/ms °C, which exceeds thermal conductivities of the biological tissues by two order of magnitude. In accordance

with (4), this forces a smaller time step for stability and thus a longer simulation when compared with the case where silicon is absent from the model. The thermal conductivity of the implant is dependent on the precise material composition of the stimulator IC, any additional supporting intraocular components, and the hermetically sealed biocompatible casing. Therefore, thermal simulations were conducted with values of $K_{\text{chip}} \in \{10, 20, 30, \ldots, 80, 90\}$, so as to characterize the dependence of temperature increase on the chip's thermal conductivity. Subsequently, in order to minimize the computational time, temperature rise associated with $K_{\text{SI}} = 150$ (corresponding to the real value of silicon) is extrapolated according to the resulting trend.

REFERENCES

[1] L. Hymen, "Epidemiology of eye diseases in the elderly," *Eye*, vol. 1, pp. 330–341, 1987.

[2] "Research to prevent blindness,", Progress Rep., 1993.

[3] Eye Care Statistics (1993). *http://spectacle.berkeley.edu/library/stats.htm#age* [Online]

[4] J. L. Stone, W. E. Barlow, M. S. Humayun, E. De Juan Jr., and A. H. Milam Jr., "Morphometric analysis of macular photoreceptor and ganglion cells in retinas with retinitis pigmentosa," *Arch. Ophthalmol.*, vol. 110, pp. 1634–1639, 1992.

[5] A. Santos, M. S. Humayun, E. De Juan Jr., R. J. Greenberg, M. J. Marsh, and A. H. Milam, "Inner retinal preservation in retinitis pigmentosa: a morphometric analysis," *Arch. Ophthalmol.*, vol. 115, pp. 511–515, 1997.

[6] M. S. Humayun, E. De Juan Jr., G. Dagnelie, R. J. Greenberg, R. H. Propst, and H. Phillips, "Visual perception elicited by electrical stimulation of the retina in blind humans," *Arch. Ophthalmol.*, vol. 114, pp. 40–46, 1996.

[7] M. S. Humayun, E. De Juan Jr., J. D. Weiland, G. Dagnelie, S. Katona, R. Greenberg, and S. Suzuki, "Pattern electrical stimulation of the human retina," *Vision Res.*, vol. 39, pp. 2569–2576, 1999.

[8] J. Wang and O. Fujiwara, "FDTD computation of temperature rise in the human head for portable telephones," *IEEE Trans. Microwave Theory Tech.*, vol. 47, pp. 1528–1534, Aug. 1999.

[9] P. Bernardi, M. Cavagnaro, S. Pisa, and E. Piuzzi, "Specific absorption rate and temperature increases in the head of a cellular-phone user," *IEEE Trans. Microwave Theory Tech.*, vol. 48, pp. 1118–1126, July 2000.

[10] O. P. Gandhi, G. Lazzi, and C. M. Furse, "Electromagnetic absorption in the human head and neck for mobile telephones at 835 and 1900 MHz," *IEEE Trans. Microwave Theory Tech.*, vol. 44, pp. 1884–1897, Oct. 1996.

[11] A. Hirata, S. I. Matsuyama, and T. Shiozawa, "Temperature rises in the human eye exposed to EM waves in the frequency range 0.6–6 GHz," *IEEE Trans. Electromagn. Compat.*, vol. 42, pp. 386–393, Nov. 2000.

[12] A. Hirata, U. Ushio, and T. Shiozawa, "Formation of hot spots in the human eye for plane wave exposures," in *Proc. Asia Pacific Microwave Conf.*, vol. 2, 1999, pp. 477–480.

[13] P. Bernardi, M. Cavagnaro, S. Pisa, and E. Piuzzi, "SAR distribution and temperature increase in an anatomical model of the human eye exposed to the field radiated by the user antenna in a wireless LAN," *IEEE Trans. Microwave Theory Tech.*, vol. 46, pp. 2074–2082, Dec. 1998.

[14] J. A. Scott, "The computation of temperature rises in the human eye induced by infrared radiation," *Phys. Med. Biol.*, vol. 33, no. 2, pp. 243–257, 1988.

[15] A. Taflove and M. E. Brodwin, "Computation of the electromagnetic fields and induced temperatures within a model of the microwave-irradiated human eye," *IEEE Trans. Microwave Theory Tech.*, vol. MTT-23, pp. 888–896, Nov. 1975.

[16] G. Lazzi, O. P. Gandhi, and D. Sullivan, "Use of PML absorbing layers for the truncation of the head model in cellular telephone simulations," *IEEE Trans. Microwave Theory Tech.*, vol. 48, pp. 2033–2039, Nov. 2000.

[17] D. Sullivan, *Electromagnetic Simulation Using the FDTD Method*. New York: IEEE Press, 2000.

[18] F. Bardati, G. Gerosa, and P. Lampariello, "Temperature distribution in simulated living tissues irradiated electromagnetically," *Alta Frequenza*, vol. XLIX, no. 2, pp. 61–67, 1980.

[19] K. P. Esselle and M. A. Stuchly, "Neural stimulation with magnetic fields: analysis of induced electric fields," *IEEE Trans. Biomed. Eng.*, vol. 39, pp. 693–700, July 1992.

[20] S. C. DeMarco, S. M. Clements, and W. Liu, "A 60 channel implantable neuro-stimulator for an epi-retinal visual prosthesis,", unpublished.

[21] A. B. Majji, M. S. Humayun, J. D. Weiland, S. Suzuki, S. A. D'Anna, and E. De Juan Jr., "Long-term histological and electrophysiological results of an inactive epi-retinal electrode array implantation in dogs," *Inv. Ophthalmol. Visual Sci.*, vol. 40, no. 9, pp. 2073–2081, Aug. 1999.

[22] S. H. Schwartz, *Visual Perception: A Clinical Orientation*. Norwalk, CT: Appleton & Lange, 1994.

[23] M. Salzmann, *The Anatomy and Physiology of the Human Eyeball is the Normal State*. Chicago, IL: Univ. of Chicago Press, 1912.

[24] The visible human project (2000). *http://www.nlm.nih.gov/research/visible/visible_human.html* [Online]

[25] Dielectric properties of body tissue*http://safeemf.iroe.fi.cnr.it/tissprop/* [Online]

[26] Compilation of the dielectric properties of body tissues at RF and microwave frequencies, C. Gabriel and S. Gabriel. *http://www.brooks.af.mil/AFRL/HED/hedr/reports/dielectric/home.html* [Online]

[27] C. Gabriel, "Compilation of the dielectric properties of body tissues at RF and microwave frequencies," Radiofrequency Radiation Division, Brooks Air Force Base, Rep. N.AL/OE-TR-1996-0037, June 1996.

[28] C. Gabriel, S. Gabriel, and E. Corthout, "The dielectric properties of biological tissues: I. Literature survey," *Phys. Med. Biol.*, vol. 41, pp. 2231–2249, 1996.

[29] S. Gabriel, R. W. Lau, and C. Gabriel, "The dielectric properties of biological tissues: II. Measurements in the frequency range 10 Hz to 20 GHz," *Phys. Med. Biol.*, vol. 41, pp. 2251–2269, 1996.

[30] ——, "The dielectric properties of biological tissues: III. Parametric models for the dielectric spectrum of tissues," *Phys. Med. Biol.*, vol. 41, pp. 2271–2293, 1996.

[31] F. A. Duck, *Physical Properties of Tissues: A Comprehensive Reference Book*. New York: Academic, 1990.

[32] *Radiofrequency Radiation Dosimetry Handbook*, 4th ed., USAF School of Aerospace Medicine, New York, Oct. 1986.

[33] M. A. Stuchly and S. S. Stuchly, "Dielectric properties of biological substances-tabulated," *J. Microwave Power*, vol. 15, pp. 19–26, 1980.

[34] J. J. W. Lagendijk, "A mathematical model to calculate temperature distributions in human and rabbit eyes during hypertermic treatment," *Phys. Med. Biol.*, vol. 27, no. 11, pp. 1301–1311, 1982.

[35] J. Hardy, A. Gagge, and J. Stolwijh, Eds., *Physiological and Behavioral Temperature Regulation*. New York: Thomas, 1970, pp. 281–301.

[36] P. Bard, Ed., *Medical Physiology*, 11th ed. St. Louis, MO: Mosby, 1961, p. 240.

[37] H. N. Kritikos, K. R. Foster, and H. P. Schwan, "Temperature profiles in spheres due to electromagnetic heating," *J. Microwave Power*, vol. 16, no. 3/4, pp. 327–344, 1981.

[38] WebElements Periodic Table (2000). *http://www.webelements.com* [Online]

[39] T. Saude, *Ocular Anatomy and Physiology*. Oxford, U.K.: Blackwell Scientific, 1993.

[40] J. Forrester, A. Dick, P. McMeneman, and W. Lee, *The Eye: Basic Sciences in Practice*. London, U.K.: W. B. Saunders, 1996.

[41] J. E. Dowling, *The Retina: An Approachable Part of the Brain*. Cambridge, MA: Belknap, 1987.

[42] Q. Li, G. Kang, and O. P. Gandhi, "A thermal model of the human head for exposure to EM fields of cellular telephones,", 1999.

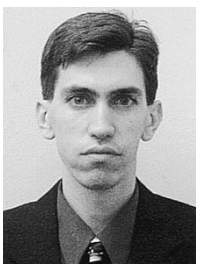

Stephen C. DeMarco was born in Fairmont, WV, in 1971. He received the B.S. *(summa cum laude)* and M.S. degrees in computer engineering from North Carolina State University, Raleigh, in 1994 and 1996, respectively, where he is currently pursuing the Ph.D. degree in electrical engineering.

His research is in the areas of analog/digital/mixed-mode circuit design, VLSI, FPGAs, and computer vision/image-processing applicable to retina prosthesis development.

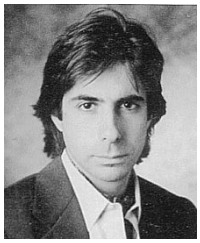

Gianluca Lazzi (S'94–M'95–SM'99) was born in Rome, Italy, on April 25, 1970. He received the Dr.Eng. degree in electronics from the University of Rome La Sapienza, Rome, Italy, in 1994 and the Ph.D. degree in electrical engineering from the University of Utah, Salt Lake City, in 1998.

He has been a Consultant for several companies (1988–1994), Visiting Researcher at the Italian National Board for New Technologies, Energy, and Environment (ENEA) (1994), Visiting Researcher at the University of Rome La Sapienza (1994–1995), and Research Associate (1995–1998) and Research Assistant Professor (1998–1999) at the University of Utah. He is presently an Assistant Professor at the Department of Electrical and Computer Engineering, North Carolina State University, Raleigh. He is author or coauthor of more than 70 international journal articles or conference presentations on FDTD modeling, dosimetry, and bioelectromagnetics.

Dr. Lazzi received a 2001 NSF CAREER Award, a 2001 Whitaker Foundation Biomedical Engineering Grant for Young Investigators, a 1996 International Union of Radio Science (URSI) Young Scientist Award, and the 1996 Curtis Carl Johnson Memorial Award for the best student paper presented at the eighteenth annual technical meeting of the Bioelectromagnetics Society. He is an Associate Editor for the IEEE ANTENNAS AND WIRELESS PROPAGATION LETTERS. He is listed in *Who's Who in the World*, *Who's Who in America*, *Who's Who in Science and Engineering*, *Dictionary of International Biographies*, and *2000 Outstanding Scientists of the 20th Century.*

Wentai Liu (S'78–M'81–SM'93) received the Ph.D. degree in computer engineering from the University of Michigan at Ann Arbor in 1983.

He has been since 1983 on the Faculty of North Carolina State University, Raleigh, where he is currently the Alcoa Professor of Electrical and Computer Engineering. His research focuses on retinal prosthesis to restore eyesight for the blind, molecular electronics, analog and digital VLSI design and CAD, phase-locked-loop, noise characterization and modeling, timing/clock optimization, high-speed transceiver for communication network, digital CMOS camera, telemetry design, and microelectronic sensor design.

Prof. Liu received an IEEE Outstanding Paper Award in 1986 and the Alcoa Foundation's Distinguished Engineering Research Award in 1999.

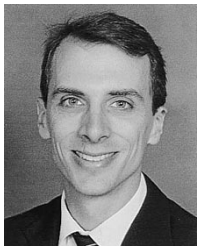

James D. Weiland (S'92–M'99) received the B.S. degree, the M.S. degree in biomedical engineering and electrical engineering, and the Ph.D. degree in biomedical engineering from the University of Michigan, Ann Arbor, in 1988, 1993, 1995, and 1997, respectively.

From 1997 to 2001, he was with the Wilmer Ophthalmological Institute, Johns Hopkins University, first as a Postdoctoral Fellow and then as an Assistant Professor. In 2001, he became an Assistant Professor in the Department of Ophthalmology, University of Southern California Keck School of Medicine, Doheny Eye Institute, Los Angeles, CA. His interests include retinal prostheses, electrode technology, visual evoked responses, and implantable electrical systems.

Dr. Weiland is a Member of the IEEE EMBS, the Biomedical Engineering Society, and the Association for Research in Vision and Ophthalmology.

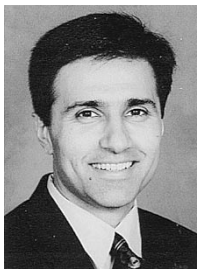

Mark S. Humayun (M'97) received the M.D. degree from Duke University, Durham, NC, in 1989 and the Ph.D. degree in biomedical engineering from the University of North Carolina, Chapel Hill, in 1993.

He has been Assistant and Associate Professor at the Department of Ophthalmology, Johns Hopkins Hospital, Baltimore, MD. He is currently a Professor in the Department of Ophthalmology, University of Southern California Keck School of Medicine, Doheny Eye Institute, Los Angeles, CA.